Published in partnership with FCT NOVA with the support of E-MRS



https://doi.org/10.1038/s41699-025-00563-3

# Understanding the origin of superconducting dome in electron-doped MoS<sub>2</sub> monolayer

Check for updates

Nina Girotto Erhardt¹⊠, Jan Berges², Samuel Poncé³,⁴ & Dino Novko¹⊠

We investigate the superconducting properties of molybdenum disulfide (MoS $_2$ ) monolayer across a broad doping range, successfully recreating the so far unresolved superconducting dome. Our first-principles findings reveal several dynamically stable phases across the doping-dependent phase diagram. We observe a doping-induced increase in the superconducting transition temperature  $T_c$ , followed by a reduction in  $T_c$  due to the formation of charge density waves (CDWs), polaronic distortions, and structural transition from the H to the 1T' phase. Our work reconciles various experimental observations of CDWs in MoS $_2$  with its doping-dependent superconducting dome structure, which occurs due to the 1 × 1 H to 2 × 2 CDW phase transition.

Novel two-dimensional (2D) materials exhibit unparalleled and highly tailorable physical and chemical properties, making them appealing for both fundamental and technological reasons<sup>1,2</sup>. With a rich diversity of phases, including superconducting (SC)<sup>3–9</sup>, ferroelectric<sup>10,11</sup>, (anti)ferromagnetic<sup>12,13</sup>, charge density wave (CDW)<sup>14,15</sup>, topological insulator<sup>16</sup>, and excitonic insulator<sup>17</sup>, all reachable by tuning temperature, pressure or doping, it is of great interest to understand the phase diagrams of 2D materials.

Molybdenum disulfide (MoS<sub>2</sub>) is a quasi-2D layered semiconducting transition-metal dichalcogenide (TMD) well known for its exceptional optical properties and strong excitonic features 18,19. When doped with excess electrons, MoS2 exhibits a complex, yet largely unexplored phase diagram, including various structural phases and many-body features such as multivalley superconductivity<sup>3,20,21</sup>, Holstein polarons<sup>22-25</sup>, and CDWs<sup>14,26-28</sup>. The ground state of the MoS<sub>2</sub> monolayer is the 1×1 H phase, with a characteristic graphene-like hexagonal structure. Mechanically and chemically exfoliated MoS<sub>2</sub> samples differ in structure. While the former results in the  $1 \times 1$  H structure, in the latter, multiple phases coexist <sup>29–34</sup>, such as 1T and 1T' phases with various periodicities<sup>28,35</sup>, mostly due to doping-induced structural modifications. Recently, a CDW phase with  $2 \times 2$  and  $2\sqrt{3} \times 2\sqrt{3}$  reconstructions was shown to exist in potassium-intercalated  $MoS_2^{14}$ . Intriguingly, the SC transition temperature  $T_c$  in electron-doped MoS<sub>2</sub> follows a characteristic dome structure<sup>3,36</sup>, resembling the phase diagrams of other unconventional correlated materials such as high- $T_c$ copper oxides<sup>37</sup>, iron-based pnictides and chalcogenides<sup>38</sup>, SrTiO<sub>3</sub><sup>39</sup>, 1T-TiSe<sub>2</sub><sup>4</sup>, and Weyl semimetals WTe<sub>2</sub><sup>40</sup> or MoTe<sub>2</sub><sup>41</sup>. Even though the SC mechanism in MoS<sub>2</sub> is well studied for lower carrier concentrations and is understood in terms of multi-valley phonon-mediated pairing<sup>20,27</sup>, the origin of the dome structure is still unresolved. Along with the various coexisting many-body interactions, the presence of polarons, CDWs, and the H to 1T' structural phase transition all inherently change the structure of MoS<sub>2</sub>, such that reconstructing a doping-dependent SC dome in MoS<sub>2</sub> is theoretically challenging. For the aforesaid systems hosting a SC dome, several mechanisms leading to a dome formation have been discussed in the literature, including the doping-induced Lifshitz transition in the Fermi surface<sup>20</sup>, the parametrization of McMillan's formula for  $T_c^{26}$ , anharmonic damping close to the phase transitions<sup>42</sup>, soft-phononmediated pairing<sup>43-46</sup>, and dynamical electron-electron interaction<sup>47</sup>. Interestingly, the impact of a doping-induced change of structure on  $T_c$  has not yet been investigated in MoS<sub>2</sub>, even though CDW and SC phases seem to coexist. It is not clear whether CDW supports or suppresses an SC phase<sup>15,48–52</sup>, but both phases employ the same conduction electrons. As the CDW phase is suppressed, the electronic density of states (DOS) at the Fermi level increases. Consequently, the SC phase is able to receive more electrons for an SC condensate. In general, this results in a simultaneous reduction of a CDW  $T_c$  and an increase of a SC  $T_c^{4,53-55}$ , and it could provide a valid explanation for the SC dome in the CDW systems such as MoS<sub>2</sub>.

Theoretical endeavors, which include electron-phonon coupling (EPC) calculations of SC  $T_c$  in the  $1\times 1$  H-MoS $_2$  phase within the isotropic Migdal–Eliashberg formalism $_c^{56}$ , McMillan's formula $_c^{57}$ , or the Allen–Dynes formula $_c^{58}$ , lead to large EPC constants and  $T_c$ 's $_c^{20,26,59}$ . These results could be improved by including anharmonic effects, which would lower the  $T_c$  and delay the onset of CDW $_c^{60}$ , while the anisotropic Migdal–Eliashberg

<sup>1</sup>Centre for Advanced Laser Techniques, Institute of Physics, 10000 Zagreb, Croatia. <sup>2</sup>U Bremen Excellence Chair, Bremen Center for Computational Materials Science, and MAPEX Center for Materials and Processes, Universität Bremen, 28359 Bremen, Germany. <sup>3</sup>European Theoretical Spectroscopy Facility, Institute of Condensed Matter and Nanosciences, Université catholique de Louvain, Chemin des Étoiles 8, B-1348 Louvain-la-Neuve, Belgium. <sup>4</sup>WEL Research Institute, avenue Pasteur 6, 1300 Wavre, Belgium. ⊠e-mail: ngirotto@ifs.hr; dino.novko@gmail.com

formalism might be important for  $MoS_2$  and low-dimensional systems<sup>61</sup>. These effects were recently taken into account, while the doping mechanism was included in a field-effect configuration<sup>62</sup>, which resulted in the accurate prediction of a SC  $T_G$  and a suppression of the EPC constant by an order of magnitude. However, in that study, the SC dome was not found, and the existence of CDW in the experimental doping range was ruled out.

Here, we conduct a comprehensive first-principles investigation of the doping-dependent phase diagram of MoS2 and find various stable phases across a large doping range. Structural changes of MoS<sub>2</sub> lead to a dome structure of the SC  $T_c$  and encompass the experimental findings of a SC dome and CDW phase. We perform nonadiabatic EPC calculations<sup>63-65</sup>, and find that it leads to a considerable reduction compared to the adiabatic EPC constants and  $T_c$ . Moreover, we find that  $T_c$  can be further lowered by taking spin-orbit coupling (SOC) into account, which is known to determine the possible pairing symmetries<sup>66</sup> and to enhance the upper critical magnetic field<sup>67-69</sup>. With this study, we successfully fill in the missing gap in comprehending the complicated phase diagram of MoS<sub>2</sub>. We show that the  $T_c$ increases for the original H phase and reaches a maximum value in a region where a normal H phase and 2 × 2 CDW coexist. For even larger doping concentrations, the 1T' phase and  $2 \times 2$  CDW ordering are stabilized with  $T_c$ being lowered, which in total forms a characteristic dome structure as observed in the experiments<sup>3,36</sup>. Our model calculations based on the tightbinding approximation (TBA)<sup>70</sup> confirm the dome structure of  $T_{\mathcal{O}}$  and additionally reveal localized polaronic distortions for carrier concentrations in the phase diagram where neither the original  $1 \times 1$  H structure nor the  $2 \times 2$  CDW phase are stable. We rely on the jellium model for doping, which leads to the overestimation of the  $T_c$  values<sup>62</sup>. Anharmonicity is neglected in this work but is important in proximity to a structural phase transition, to determine the exact critical doping at which a CDW transition occurs. However, the qualitative explanation of the dome structure origin in MoS<sub>2</sub> related to structural transitions provided in this work remains valid even if anharmonicity shifts the dome to a different doping region, and if taking a gating geometry into account.

# Results

MoS<sub>2</sub> can be doped by gating or intercalation, reaching large charge densities. In Fig. 1, we show a doping-dependent phase diagram of dynamically

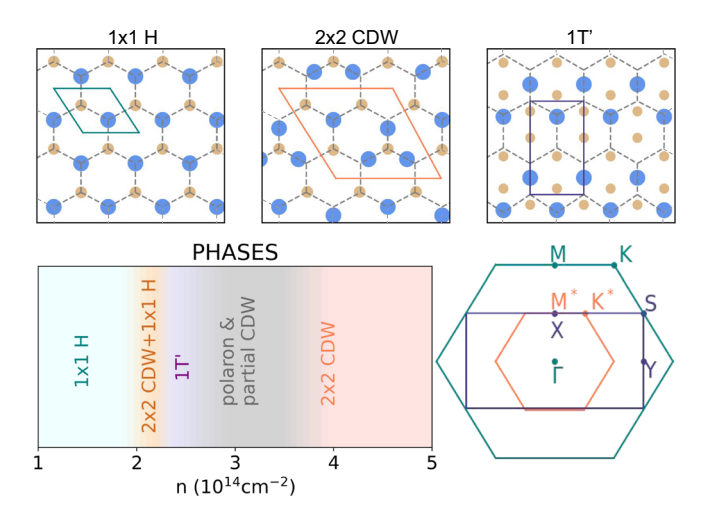


Fig. 1 | Phase diagram of electron-doped  $MoS_2$  with various dynamically stable phases. In the upper row, we show the three distinct phases appearing in the phase diagram together with their primitive cells. For visualization, the atomic structures are shown with exaggerated atomic displacements (ten times) and on top of a hexagonal mesh. Each of the phases from the first row is stable in some doping range, as color-coded in the phase diagram. For the gray shaded area, our TBA model predicts the stabilization of polaronic distortions and partial CDWs. The corresponding Brillouin zones are displayed in the second row with the same color code from the phase diagram.

stable structures that  $MoS_2$  assumes, as obtained from density functional theory (DFT), including the  $1 \times 1$  H phase,  $2 \times 2$  CDW structure with distorted atoms, and 1T' phase. Between the regions where the 1T' and high-doping  $2 \times 2$  CDW phases are stable, our TBA simulations reveal polaronic distortions and partial CDW coverage. Our aim is to calculate the EPC strengths and  $T_c$  across these phase transitions.

#### The low-doping 1 x 1 H phase

Our calculated phonon dispersions indicate a dynamically stable  $1 \times 1~\mathrm{H}$ structure up to the excess charge concentration of  $2.38 \times 10^{14}$  cm<sup>-2</sup>, when the acoustic phonon of A<sub>1</sub> symmetry at the M point of the Brillouin zone (BZ), shown in Fig. 2a, induces the instability. This critical doping  $n_c$  is sensitive to the choice of the electronic temperature in the DFT electronic structure calculations, and varies from  $n_c = 1.5 \times 10^{14} \,\mathrm{cm}^{-2}$  $n_c = 2.4 \times 10^{14} \,\mathrm{cm}^{-2}$  when  $T_{\rm scf}$  is between 100 and 800 K, as one can see in Supplementary Figs. 1, 2. Here we use  $T_{\rm scf}$  = 800 K since the choice of a lower electronic temperature would require denser momentum grids. This strongly coupled acoustical phonon describes the motion of Mo atoms towards the S atom, and by increasing doping, its frequency softens. Its strong coupling to electrons manifests itself as a large broadening in the phonon spectral function  $B_{\nu}(\mathbf{q}, \omega)$  [see Fig. 2b] and as a large peak in the Eliashberg spectral function  $\alpha^2 F(\omega)$  [see Fig. 2c]. Here we also show how the  $\alpha^2 F(\omega)$  and the EPC constant  $\lambda$  in a nonadiabatic (NA) formalism (see Methods) differ from their adiabatic (A) counterparts<sup>63</sup>. With the largest contribution coming from the A<sub>1</sub> soft mode, the NA frequency renormalization and broadening effects strongly renormalize the EPC properties. In fact, the NA effects reduce the EPC strength  $\lambda$  by half, which mostly comes from the blueshifted Kohn anomalies at the M and K points of the BZ. In the second row of Fig. 2, we show doping-dependent quantities calculated from the NA phonon spectrum.

The doping-dependent EPC constant  $\lambda$  and the corresponding  $\omega_{\log}$  for the  $1\times 1$  H stable part of the phase diagram in Fig. 2d form a dome, but we rule out the possibility that the SC dome arises due to  $\omega_{\log}$  in the  $T_c$  formula<sup>26</sup>. In fact, we find that the  $T_c$  is monotonically increasing according to McMillan's formula, the Allen–Dynes formula, as well as the isotropic Migdal–Eliashberg formalism in agreement with ref. 62 [see Fig. 2e]. For the two largest dopings, we show how the inclusion of the SOC lowers the  $T_c$  by ~30%. An increase of the Coulomb pseudopotential  $\mu^*$  can also reduce the value of  $T_c$  by a few percent (see Supplementary Fig. 3). Note that our computed  $T_c$  values overestimate the experiments, and that more quantitative results would be obtained with the additional inclusion of anharmonicity and proper gating geometry<sup>62</sup>.

#### Coexistence of 2 × 2 CDW and 1× 1 H phases

Slightly before the instability, we find that a  $1 \times 1$  H structure coexists with a  $2 \times 2$  CDW phase. In analogy to the  $1\text{T-TiSe}_2^{-7}$ , our calculations show that the CDW in  $\text{MoS}_2$  is driven by three nonequivalent M phonon instabilities and results in a  $2 \times 2$  unit cell with triangular distortions of Mo atoms [see Figs. 1, 2a as well as Supplementary Fig. 4], in agreement with the CDW pattern found in the recent STM measurements <sup>14</sup>. Due to the splitting of the bands [see Fig. 3a], the DOS at the Fermi level in a  $2 \times 2$  CDW phase drops, making it energetically favorable. However, due to the existence of the two minima in the potential energy surface [see Fig. 3c], the atom relaxation in a  $2 \times 2$  supercell results in a hysteresis loop as doping is varied [see Fig. 3d].

For the same critical doping value, we find that the  $1 \times 1$  H structure becomes unstable due to the aforementioned M point phonon instability, while a  $2 \times 2$  CDW structure becomes unstable due to the M\* point (see Fig. 1) phonon instability. The latter is clearly visible in Fig. 3e. In the  $1 \times 1$  H phase, the M point instability is a result of electronic transitions between the filled K and 1/2 K electron pockets on the Fermi surface. In the  $2 \times 2$  CDW phase, band splitting leads to the occurrence of the flat band close to the Fermi level at the M point. Electron transitions between these flat-band parts cause phonon softening in the new backfolded M\* point (see Supplementary Fig. 5).

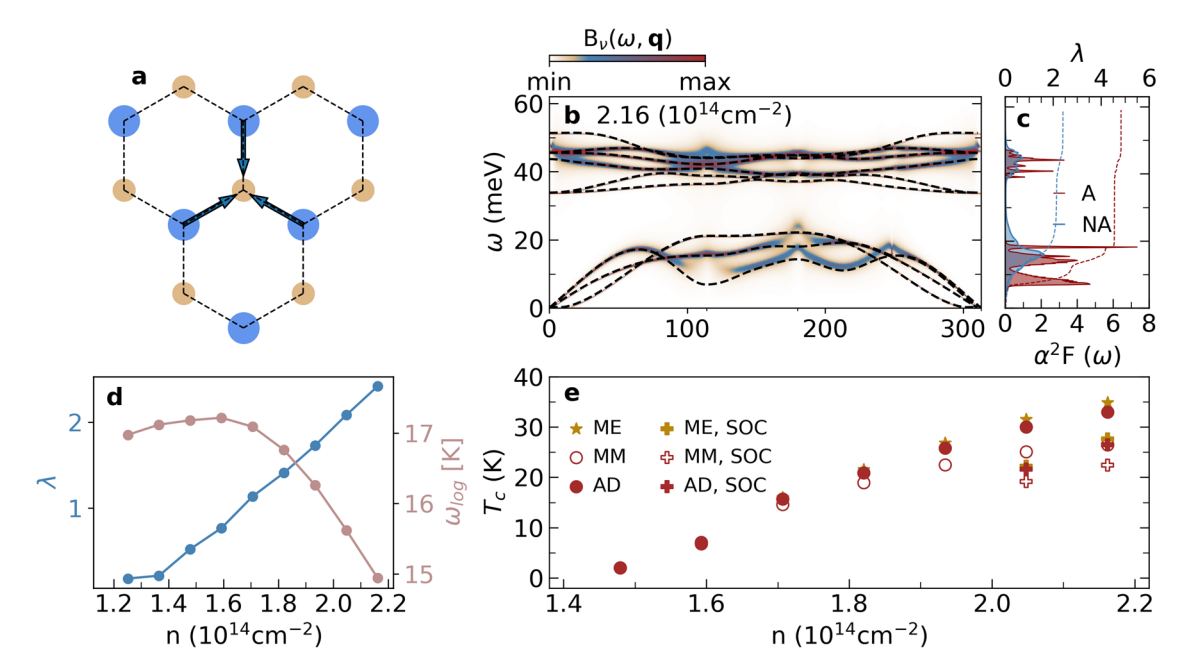


Fig. 2 | Electron-phonon properties of  $MoS_2$  in the  $1 \times 1$  H phase. a Schematics of the linear combination of the strongly coupled lowest-energy acoustic phonon eigendisplacements of  $A_1$  symmetry at all  $\mathbf{q} = M$  points, see Supplementary Fig. 3. b Phonon spectral function of  $MoS_2$  at 800 K, with the adiabatic phonon band structure denoted with dashed black line. c Eliashberg spectral function in the adiabatic (A, red) and nonadiabatic (NA, blue) approximations together with the

corresponding EPC cumulative constant  $\lambda(\omega)$ . **d** EPC strength  $\lambda$  and logarithmic average frequency  $\omega_{\log}$  computed with NA phonons. **e** Superconducting  $T_c$  calculated using McMillan's (MM) formula (hollow red circles), the Allen–Dynes (AD) formula (full red dots), and the isotropic Migdal–Eliashberg (ME) formalism (golden stars). Cross symbols denote the calculations which include spin–orbit coupling.

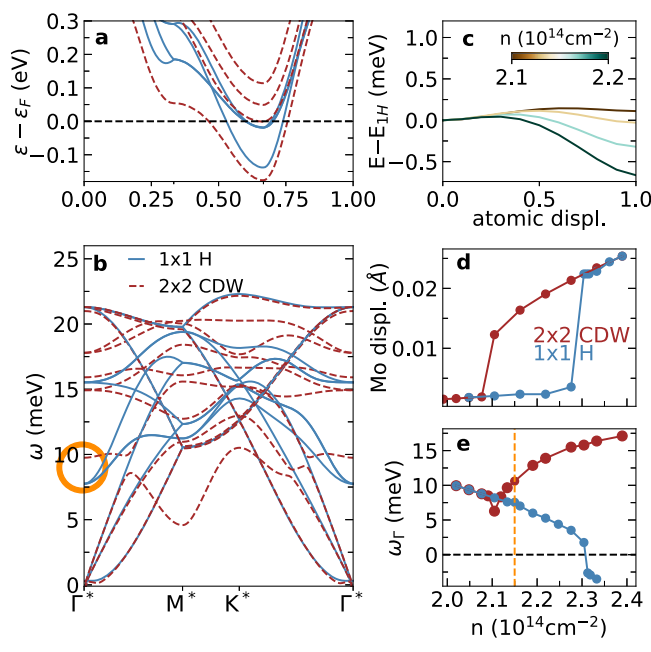


Fig. 3 | Coexistence of the  $1 \times 1$  H and  $2 \times 2$  CDW phases and corresponding electron and phonon properties. a Electron band structures comparison of the two phases for  $n = 2.15 \times 10^{14}$  cm<sup>-2</sup>. b Phonon dispersion comparison, with the soft mode from (e) denoted with an orange circle. c Potential energy surface between the two phases for a range of different dopings. d Hysteresis plot of the doping-dependent displacement of the Mo atoms. e Doping-dependent frequency of the  $\Gamma^*$  mode, backfolded from the M point of the  $1 \times 1$  unit cell. The orange vertical line corresponds to  $n = 2.15 \times 10^{14}$  cm<sup>-2</sup>. See Fig. 1 for the definition of the starred (\*) high-symmetry points.

#### The 1T' phase

Next, we find that one possible stable structure for larger doping values is a 1T' phase, which is separated from the  $1 \times 1$  H phase by a large energy

barrier of around 10 eV. This could explain why the transition to the 1T' phase in experiments is not observed when MoS<sub>2</sub> is doped by gating  $^{32,72,73}$ . The 1T' phase is a metastable phase, and our calculations confirm that the barrier reduces by doping  $^{74}$  (see Supplementary Fig. 6). We stress that the unit cell of the 1T' phase for this doping region is not related to the  $\omega_{\rm M}$  instability in the 1 × 1 H structure nor the  $\omega_{\rm M^*}$  instability in the 2 × 2 CDW structure, but we find it to be dynamically stable for this doping regime. In Fig. 4a we show the electronic bands and find that the 1T' phase is stable for a narrow doping region which could be a consequence of its Fermi surface, which is prone to nesting (see Supplementary Fig. 7). The phonon dispersion in Fig. 4b reveals many Kohn anomalies in the lowest acoustic branch, appearing for the wave vectors which nest the Fermi surface. Again, we observe large NA effects in the EPC properties [see Fig. 4c].

## Polaronic distortions and partial CDW

Remarkably, after the  $1\times 1$  H structure reaches instability, it does not immediately stabilize into the  $2\times 2$  CDW phase. As the  $1\times 1$  M point backfolds in the  $2\times 2$   $\Gamma$  point, a  $2\times 2$  CDW phase seems to stabilize this particular instability [see Fig. 3e] but, as demonstrated above, only for the narrow doping region from 2.11 to  $2.38\times 10^{14}\, cm^{-2}$ . By adding more electrons, this  $2\times 2$  CDW phase again shows an instability in the new M\* point (see Supplementary Fig. 5), suggesting the existence of structural distortions on a larger length scale.

Calculations with supercells larger than  $2 \times 2$  are expensive within DFT and, therefore, we use a TBA model to investigate the region of our phase diagram where neither H nor  $2 \times 2$  CDW phases are stable (see gray area in Fig. 1). Our model calculations show that stable structures indeed require much larger supercells, once the doping is increased past the first instability point. Considering an  $18\sqrt{3} \times 18\sqrt{3}$  supercell, we find a single localized distortion, a polaron, where the triangular displacement of the three Mo atoms resembles that of a single unit of the  $2 \times 2$  CDW in Fig. 2a. With increasing doping, the number of localized distortions increases, forming first a partial and then a full  $3\sqrt{3} \times 3\sqrt{3}$  CDW.

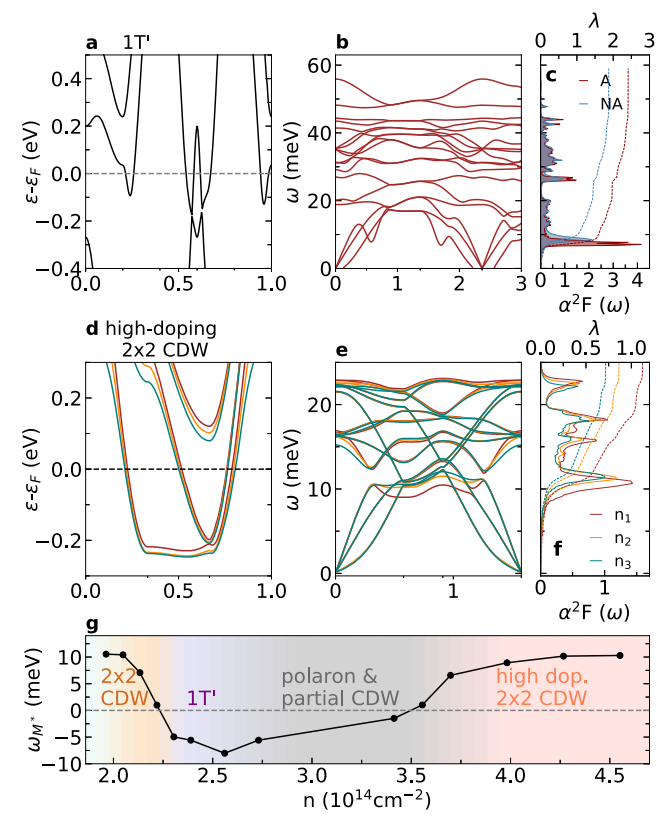


Fig. 4 | Properties of MoS<sub>2</sub> in the 1T' and high-doping  $2 \times 2$  CDW phases. a Electron band structure obtained for the excess charge of  $n = 2.62 \times 10^{14}$  cm<sup>-2</sup>. b Adiabatic phonon dispersion. c Eliashberg spectral function calculated using the adiabatic (A) and nonadiabatic (NA) formula, with the corresponding cumulative EPC constant  $\lambda(\omega)$ . d Electron band structures for the largest doping values considered in this work;  $n_1 = 3.0 \times 10^{14}$  cm<sup>-2</sup>,  $n_2 = 4.3 \times 10^{14}$  cm<sup>-2</sup>,  $n_3 = 4.6 \times 10^{14}$  cm<sup>-2</sup>. e Corresponding phonon dispersions and f NA Eliashberg spectral functions with cumulative EPC constants  $\lambda(\omega)$ . g Softening and stabilization of the M\* point acoustic phonon. The stabilization of this mode defines the low- and high-doping  $2 \times 2$  CDW phase, while the region where it is unstable corresponds to the polaronic and partial CDW phases.

## The high-doping 2 x 2 CDW phase

At high doping, our DFT calculations show that a  $2 \times 2$  CDW phase once again becomes stable. The soft acoustic phonon at the M\* point of the  $2 \times 2$  BZ visible in Fig. 3b starts to blueshift as a function of doping, and becomes stable for around  $n = 3.5 \times 10^{14}$  cm<sup>-2</sup>, as depicted in Fig. 4g. The flattening of the lowest conduction band, which hosts the excess charge [see Fig. 4d], significantly lowers the DOS at the Fermi level. As doping is increased, the M\* point Kohn anomaly hardens [see Fig. 4e, g], while the EPC constant reduces.

For this doping range, we also report a  $2\sqrt{3} \times 2\sqrt{3}$  CDW phase coexistence (see Supplementary Fig. 8), in agreement with the experiment <sup>14</sup>. Here again, the triangular pattern of Mo displacements is present, but in a modulated configuration where one in three triangles is more pronounced. Even though we report the stability of a  $2\sqrt{3} \times 2\sqrt{3}$  CDW phase for much larger doping values than the doping values for which the  $1 \times 1$  H phase is dynamically stable, we note that for the  $1 \times 1$  H phase, there is an additional adiabatic Kohn anomaly close to the K point and strong nonadiabatic effects exactly at the K point [see Fig. 2b]. Since the transition from the  $1 \times 1$  H phase to the high-doping  $2 \times 2$  and  $n\sqrt{3} \times n\sqrt{3}$  CDW phases is not direct, we do not observe clear signatures for both phases in the low-doping phonon band structure, but the mentioned anomalies indicate strong EPC effects for the K point mode. We also show in Supplementary Fig. 5b the newly formed Kohn anomaly along  $\Gamma^*$ – $K^*$  path that appears for  $2 \times 2$  CDW structure in the unstable region, also indicating a potential stability of

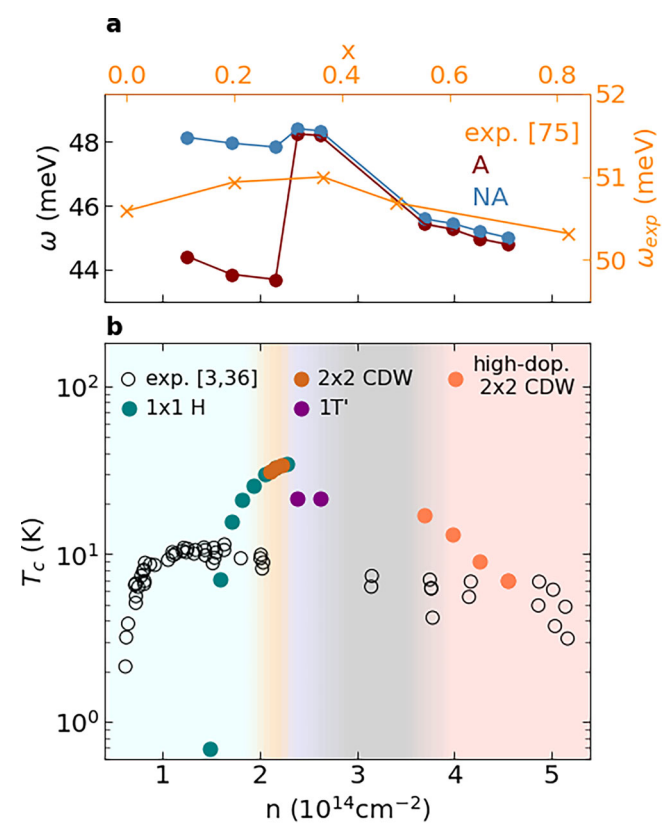


Fig. 5 | Recreating the superconductivity dome structure of  $T_c$  in doped MoS<sub>2</sub>. a Evolution of the A<sub>1</sub> phonon mode frequency across the phase transition from the  $1 \times 1$  H to the 1T' phase in the adiabatic and nonadiabatic approximation (lower x-axis). First-principles data is compared with the experiment from ref. 75, and the upper x-axis that corresponds to the experimental data is the atomic ratio of Li(x) in Li<sub>x</sub>MoS<sub>2</sub>. b Doping-dependent SC phase diagram of MoS<sub>2</sub>, with different phases color-coded in the background. The experimental results for  $T_c$  are presented with open black symbols<sup>3,36</sup>.

 $n\sqrt{3} \times n\sqrt{3}$  pattern. Using the TBA model, both a perfect  $2 \times 2$  CDW and massively distorted  $3\sqrt{3} \times 3\sqrt{3}$  CDWs are stable, indicating that there should be other competing CDW orders in the system.

## **Discussion**

To further validate the obtained structural phase diagram as a function of doping, in Fig. 5a we compare the calculated phonon frequency of Ramanactive A<sub>1g</sub> optical phonon mode across various phases with the experimental measurements done on Li-doped (i.e., electron-doped)  $MoS_2^{75}$ . This  $A_{1g}$ optical phonon is an out-of-plane mode at the center of the BZ that is strongly coupled to the excess charge carriers in the conduction valleys of  $MoS_2$ , and in the  $1 \times 1$  H phase is redshifted as a function of conduction band population  $^{65,76}$ . However, in Raman measurements, the frequency of the  $A_{1g}$  mode is blueshifted with the maximum value around x = 0.4 (where x is the ratio of Li atoms with respect to the MoS<sub>2</sub> unit), and then redshifted for x > 0.5. Our theoretical results presented in Fig. 5a confirm that the phase transitions between 1 × 1 H, 1T', and CDW phases need to be taken into account in order to qualitatively capture the observed doping-induced renormalization of A<sub>1g</sub> frequency. Additionally, the large NA frequency renormalization of the  $A_{1g}$  mode for the 1 × 1 H phase is present <sup>65,77</sup>, and it is crucial for understanding the modifications of the phonon frequency across the whole phase diagram. We observe larger nonadiabatic renormalizations in the  $1 \times 1$  H phase than in the 1T' phase or the high-doping  $2 \times 2$  CDW phase. In contrast, their strength does not change much with doping within the same phase. The change of phase impacts the band structure, modifies the electron scattering phase space, and it also leads to different EPC matrix

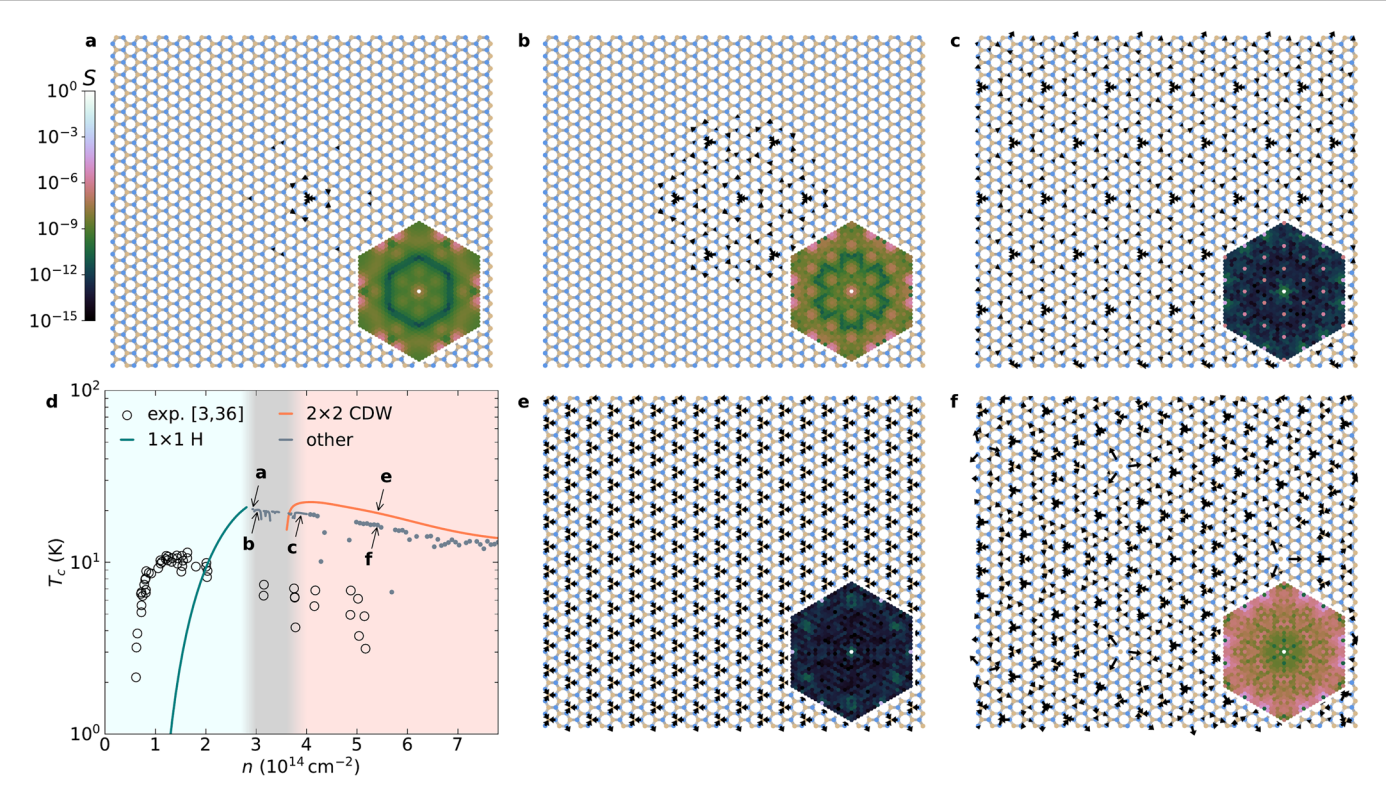


Fig. 6 | First-principles-based tight-binding model for MoS<sub>2</sub> monolayer. All calculations have been performed on an  $18\sqrt{3}\times18\sqrt{3}$  supercell, using the approximation of a linearized, nearest-neighbor EPC. Doping is modeled via a rigid shift of the chemical potential. **a–c** Transition from polaronic deformation via partial to full  $3\sqrt{3}\times3\sqrt{3}$  CDW for intermediate dopings. **d** Critical temperature according to the Allen–Dynes formula as a function of doping for different structural phases. The underlying effective parameters  $\lambda$  and  $\omega_{\log}$  as well as the energy gain and

displacement magnitude are shown in Supplementary Fig. 7. The experimental reference points are the same as in Fig. 5 and taken from refs. 3,36. e, f 2 × 2 CDW and strongly distorted phase at high doping. Arrows indicate atomic displacements, scaled by a factor of 20 for better visibility. Hexagonal insets show the structure factor  $S = |\sum_{i=1}^{N_{at}} \exp(i\mathbf{q}\mathbf{R}_i)/N_{at}|^2$  for all supercell  $\Gamma$  points  $\mathbf{q}$  inside the first Brillouin zone of the primitive  $1 \times 1$  cell, which indicates periodicities present in the shown relaxed displacement patterns.

elements. We find that weak nonadiabatic effects in the 1T' and the high-doping  $2 \times 2$  CDW phases are the result of smaller EPC matrix elements and a change in electronic scattering phase space.

In Figs. 5, 6, we show a complete phase diagram of  $MoS_2$  obtained from first principles and model calculations, respectively. Firstly, a monotonically increasing  $T_c$  with doping persists until the point of instability. In the region of  $1 \times 1$  H and  $2 \times 2$  CDW phase coexistence, we report the  $T_c$  to be almost the same in the two phases, and it reaches its peak value of 34.6 K. The bands' reconstruction in a  $2 \times 2$  CDW phase compared to the  $1 \times 1$  H phase for the same doping leads to the softening of the  $M^*$  acoustic phonon mode and a significant EPC contribution coming from the lower frequency mode. This is accompanied by changes in the electronic DOS, reaching slightly larger values in the  $1 \times 1$  H phase (see Supplementary Fig. 9). The doping-induced increase in the DOS and the softening of the  $M^*$  point acoustic phonon lead to an increase in the  $T_c$ . As the system assumes the 1T' phase, the SC  $T_c$  is lower, in agreement with experiments  $T_c$ 8.

When the  $2 \times 2$  CDW phase becomes stable again for larger doping concentrations, due to hardening of the strongly coupled mode with doping and decrease of the DOS at the Fermi level, SC  $T_c$  is reduced further. Note that the doping concentrations corresponding to the experimentally observed regions of a  $2 \times 2$  and  $2\sqrt{3} \times 2\sqrt{3}$  CDW phases<sup>14</sup> overlap with the region where the SC  $T_c$  is decreasing<sup>36</sup>. We believe that the indirect transition from the  $1 \times 1$  H phase to a  $2 \times 2$  CDW (possibly via polaronic phases) is the leading explanation of the SC dome. Good qualitative agreement with the experimental dome structure<sup>3,36</sup> further corroborates this claim. We note also that the dome structure of  $T_c$  is correlated to the softening of the M\* phonon, as one can see from Fig. 4g. See also Supplementary Fig. 9 for the interplay of DOS at the Fermi level and softening of the relevant phonon mode.

The above results are confirmed by the TBA model calculations. We emphasize that the purpose of our model is a qualitative understanding, and not to provide precise quantitative values of SC  $T_c$ . Figure 6d shows  $T_c$  as a function of doping for different stable structures on the  $18\sqrt{3} \times 18\sqrt{3}$ supercell (see Methods). In agreement with the DFT results in Fig. 5, we find that the  $1 \times 1$  H and  $2 \times 2$  CDW structures are favored for smaller and larger dopings, respectively. For intermediate dopings, however, both are unstable toward the formation of polaronic distortions and partial CDWs as shown in Fig. 6a-c. The periodicities present in these different types of structural order can be seen in the structure factor S shown in the insets. A possible explanation is that the doping electrons tend to localize near triangular distortions involving three Mo atoms, which can only cover the full sample as in the 2 × 2 CDW if enough excess charge is available. Here the TBA model calculations confirm that the saturation (or even slight decrease) of the DOS at the Fermi level for the polaronic and CDW phases, as well as the hardening of the relevant phonon modes, lead to the reduction of SC  $T_c$  (see Supplementary Fig. 10). Our previous studies of such distortions in the MoS<sub>2</sub> monolayer using the same model approach have revealed associated dispersionless in-gap states<sup>24,25</sup>. Recently, similar distortions and bands have also been predicted for photodoped MoS<sub>2</sub> and other TMDs<sup>79</sup>. Also, a recent study of bulk MoTe<sub>2</sub> argued that the laser-induced transition from 2H to 1T' phase goes through polaron formation<sup>80</sup>. Our combined DFT and TBA simulations suggest that such polaron formation might be universal and present in equilibrium conditions, playing an important role in structural phase transitions and formation of the SC dome.

Note that even though we reproduce the dome structure of  $T_c$  in accordance with the experiments, our values of  $T_c$  are always larger than the measured ones. For instance, the maximum values obtained in refs. 3,36 are  $T_c$  = 10.9 K and  $T_c$  = 11.6 K, respectively. Here we obtain  $T_c$  = 29.9 K for n = 2.04 × 10<sup>14</sup> cm<sup>-2</sup>, while this value is additionally reduced to  $T_c$  = 21.6 K

when SOC is included. In recent theoretical work, for the same doping concentration of  $n = 2.02 \times 10^{14} \,\mathrm{cm}^{-2}$ , a  $T_c = 19 \,\mathrm{K}$  was reported<sup>62</sup>, and the importance of using anharmonic corrections and a realistic gating geometry compared to a homogeneous jellium background for reaching the more quantitative  $T_c$  was discussed. In ref. 47, the renormalization of electronic states due to electron correlations was discussed as an important ingredient to obtain the quantitative agreement with the experimental  $T_c$ . It should also be noted that the onset and the maximum value of the  $T_c$  in our calculations is shifted toward larger doping concentrations compared to the experiments. For instance, the critical doping at which the  $T_c$  is maximum and where the original  $1 \times 1$  H structure becomes unstable is  $n_c = 2.1 \times 10^{14} \,\mathrm{cm}^{-2}$ , while in the experiments this value is around  $n_c = 1.5 \times 10^{14} \,\mathrm{cm}^{-2}$  3. Nevertheless, this could be corrected by using the lower value for electronic temperature in DFT calculations, see also Supplementary Fig. 1. Another important factor in determining the critical doping could also be the Mo-S distance, see Supplementary Fig. 2b, which dictates the energy ratio between the K and Q valleys in the band structure<sup>65,76</sup>, and, therefore, the onset of SC and CDW states. The energy ratio between the relevant K and Q valleys is also highly sensitive to the choice of DFT functionals. For example, the PBE functional provides the value of ~250 meV, while the many-body G<sub>0</sub>W<sub>0</sub> correction would give ~50 meV, which is closer to experimental estimations<sup>65</sup>. Interestingly, ref. 81 argues that the inclusion of quantum lattice fluctuations in pristine MoS2 reduces the energy difference between K and Q valleys compared to the adiabatic frozen calculations as obtained in the DFT. Therefore, it is possible that in the proximity to the polaronic and CDW instabilities in doped samples, these fluctuations are even stronger and also reduce the value of  $n_c$ . Further, we find that the presence of a substrate would alter the critical doping value, but would still enable a CDW transition. In the Supplementary Table 1, we report a DFPT analysis of the soft mode and we observe more pronounced softening of the M point instability when a single layer of MoS<sub>2</sub> is placed on a graphite and hBN substrates (see also Supplementary Fig. 11). Our analysis indicates that the presence of a substrate even enhances a CDW transition. Interfacial interactions between monolayer MoS<sub>2</sub> and a substrate therefore support our conclusions on the superconducting dome origin and shift it to lower doping values, closer to its experimentally observed doping region.

There are many studies discussing EPC strengths and the corresponding  $T_c$  for doped  ${\rm MoS_2}^{20,23,26,47,59,62,82,83}$ , however, the dome structure and the complete phase diagram up to higher doping concentration is rarely discussed, even though intriguing SC dome appears in many different materials, including different TMDs<sup>84</sup>.

In refs. 62,83 only the saturation of  $T_c$  as a function of doping was theoretically obtained, while it was argued that the SC dome structure observed in the experiments is due to extrinsic effects, such as charge localization for higher dopings, which leads to strong disorder and therefore to effective increase of the Coulomb electron-electron repulsion, which competes with the phonon-mediated pairing85. This was modeled phenomenologically by increasing the Coulomb repulsion parameter  $\mu^*$  that enters the Allen-Dynes formula and Eliashberg equations from 0.1 to 0.15. In ref. 47 it is claimed that an increase of electron correlations with doping is an intrinsic effect, which suppresses the EPC and, therefore, the  $T_{o}$  producing a dome structure. However, the latter studies neglect the structural phase transitions, and the corresponding modifications to the electronic structure that are clearly present in MoS<sub>2</sub> for larger doping concentrations. In another work, the SC dome structure appears due to the parametrization of McMillan's formula<sup>26</sup>, where a certain combination of EPC  $\lambda$  and  $\omega_{log}$ could result in the saturation and decrease of  $T_c$ . On the other hand, here we show that the  $T_c$  for the 1 × 1 H phase is always increasing as a function of doping (see also results in ref. 62), both for the Allen-Dynes and Migdal-Eliashberg approaches. In the same study, the CDW phase was predicted to exist in doped MoS<sub>2</sub>, but the authors only reported the  $2 \times 1$ CDW pattern coming from one nonequivalent M phonon instability, while here we report on the full 2×2 CDW phase induced by the three nonequivalent soft phonon modes. In addition, we show that this  $2 \times 2$  CDW

phase in  $MoS_2$  is not stabilized immediately after the  $1 \times 1$  H phase becomes unstable, but is preceded by the polaronic states and partial CDWs, as well as possibly by the 1T' phase. Also, the EPC strength and  $T_c$  was not evaluated beyond the  $1 \times 1$  H phase in ref. 26.

Here we show that the SC dome structure in doped MoS<sub>2</sub> is related to the strongly coupled soft phonon modes responsible for the structural phase transitions, as Figs. 3b, e, 4g, as well as the model data in Supplementary Figs. 9, 10, suggest. Namely, when approaching the point of structural instability with doping, the relevant phonon mode becomes softer, and therefore, the EPC  $\lambda$  and  $T_c$  are increased. With a further increase of doping, the new structure is stabilized, the relevant phonon mode hardens, and  $\lambda$  and  $T_c$  decrease, which in total creates the dome structure. The importance of the soft phonon modes in elevating the  $T_c$ was discussed a long time ago for A15 compounds<sup>86,87</sup>, and it was proposed as a source of the unconventional SC dome structure in SrTiO<sub>3</sub><sup>43,44</sup> as well as predicted to play a role in BaTiO<sub>3</sub><sup>46</sup> and WTe<sub>2</sub><sup>45</sup>. For SrTiO<sub>3</sub>, the critical doping concentration for which the  $T_c$  reaches maximum value correlates with the point when the optical polar phonon at the center of the BZ becomes unstable, inducing ferroelectric fluctuations<sup>44</sup>. Here, instead of the ferroelectric phase, the maximal  $T_c$  is related to the CDW and polaronic phase transitions and the corresponding soft acoustic phonon modes away from the BZ center.

In conclusion, we have explored the phase diagram of electron-doped MoS<sub>2</sub> and explained the SC dome structure observed in various transport and tunneling experiments. Across a large doping range, we have found a number of dynamically stable phases, such as the 2 × 2 CDW, the 1T' phase, polaronic states, and partial CDWs. In agreement with existing literature, we have found a doping-induced increase in  $T_c$ . Since the same strongly coupled acoustic phonon mode is responsible for the SC transition and a CDW occurrence, the doping-dependent EPC entirely coordinates their interplay. In this work, we observe that the initial rise of EPC strength with doping is followed by a corresponding increase in the superconducting  $T_{\alpha}$  favoring a superconducting state over charge ordering. However, the strong EPC eventually leads to a soft phonon mode, inducing a lattice reconstruction. Following a steep increase, a combination of structural phase transitions and CDW formations leads to its reduction. The latter correlates with the softening and hardening of the relevant acoustic phonon modes that are both responsible for the structural phase transitions and dominate the SC pairing mechanism. Comparing the EPC doping dependence in a 1 × 1 H phase and a high-doping  $2 \times 2$  CDW phase, it can be noted that the two regimes are the exact opposites of one another. In the first regime, doping induces an increase in EPC and softening of the acoustic mode, while it stabilizes the CDW in the second regime. Therefore, we can conclude that a CDW state suppresses an SC state in MoS<sub>2</sub>. Our work reconciles various experimental findings of CDWs in MoS2, with its doping-dependent SC dome structure, and could be helpful in comprehending the SC mechanism of other materials hosting a  $T_c$  dome, such as other correlated TMDs and SrTiO<sub>3</sub>.

# Methods

#### Migdal-Eliashberg theory

When it comes to calculating the  $T_{\rm o}$  there exist several levels of complexity, building up on the pioneering work of Bardeen, Cooper, and Schrieffer (BCS)<sup>88</sup>. Specific details of a material's electronic structure, phonon spectrum, and interaction strengths can be included within the scope of Migdal–Eliashberg theory<sup>56</sup>. The smoothness of the Fermi surface determines whether an isotropic set of Eliashberg equations can be used<sup>89,90</sup>:

$$\widetilde{\omega}_n = \omega_n + T \int_{-\infty}^{\infty} d\varepsilon \frac{N(\varepsilon)}{N(\varepsilon_F^0)} \sum_m \frac{\widetilde{\omega}_m}{\Theta_m(\varepsilon)} \lambda_{n-m}, \tag{1a}$$

$$\phi_n = T \int_{-\infty}^{\infty} d\varepsilon \frac{N(\varepsilon)}{N(\varepsilon_F^0)} \sum_m \frac{\phi_m}{\Theta_m(\varepsilon)} [\lambda_{n-m} - \mu], \tag{1b}$$

$$\chi_{n} = -T \int_{-\infty}^{\infty} d\varepsilon \frac{N(\varepsilon)}{N(\varepsilon_{F}^{0})} \sum_{m} \frac{\varepsilon - \varepsilon_{F} + \chi_{m}}{\Theta_{m}(\varepsilon)} \lambda_{n-m}, \qquad (1c)$$

$$n_e = \int_{-\infty}^{\infty} d\varepsilon N(\varepsilon) \left[ 1 - 2T \sum_{m} \frac{\varepsilon - \varepsilon_F + \chi_m}{\Theta_m(\varepsilon)} \right], \quad (1d)$$

with the common denominator

$$\Theta_n(\varepsilon) = \widetilde{\omega}_n^2 + \phi_n^2 + [\varepsilon - \varepsilon_E + \gamma_n]^2. \tag{1e}$$

Here,  $N(\varepsilon)$  is the DOS per spin,  $\omega_n = (2n+1)\pi T$  are fermionic Matsubara frequencies,  $\widetilde{\omega}_n$  are renormalized Matsubara frequencies,  $\phi_n$  is the SC order parameter, and  $\chi_n$  an energy shift. The number of electrons  $n_\varepsilon$  is conserved, which implies that the chemical potential  $\varepsilon_F$  may deviate from its noninteracting value  $\varepsilon_F^0$ . The Eliashberg equations are solved iteratively for  $\widetilde{\omega}_n$ ,  $\phi_n$ ,  $\chi_n$ , and  $\varepsilon_F$ , using our own implementation<sup>91</sup>. The presence of an SC state  $(\phi_n > 0)$  for a given temperature T is determined by the effective Coulomb interaction  $\mu$  and the effective EPC

$$\lambda_n = \int_0^\infty d\omega \frac{2\omega}{\omega^2 + \nu_n^2} \alpha^2 F(\omega), \tag{2}$$

where  $v_n = 2n\pi T$  are bosonic Matsubara frequencies. Since we are only interested in the value of  $T_o$  it is sufficient to only consider the linearized version  $(\phi_n \to 0)$  of the equations.

From the linearized form of the (real-axis) Eliashberg equations, McMillan's formula can be qualitatively obtained<sup>57</sup>. The majority of theoretical estimates of  $T_c$  rely on McMillan's semiempirical result, which was later refined by Allen and Dynes<sup>58</sup>:

$$T_c = \frac{f_1 f_2 \omega_{\log}}{1.2} \exp\left[-\frac{1.04(1+\lambda)}{\lambda - \mu^* - 0.62\lambda\mu^*}\right].$$
 (3)

The strong-coupling correction  $f_1=\left[1+(\lambda/\Lambda_1)^{3/2}\right]^{1/3}$  and the shape correction  $f_2=1+(r-1)\lambda^2/(\lambda^2+\Lambda_2^2)$  with  $\Lambda_1=2.46(1+3.8~\mu^*)$ ,  $\Lambda_2=1.82(1+6.3~\mu^*)r$ , and  $r=\overline{\omega}_2/\omega_{\log}$  are needed if  $\lambda>1.5$ . We refer to Eq. (3) as the Allen–Dynes formula, while the same result without the strong-coupling corrections is referred to as McMillan's formula. EPC effects are encapsulated in the EPC constant  $\lambda$  and the logarithmic and second-moment average phonon frequencies  $\omega_{\log}$  and  $\overline{\omega}_2$ , which are obtained as integrals over the Eliashberg spectral function:

$$\lambda = 2 \int_0^\infty \frac{\alpha^2 F(\omega)}{\omega} d\omega = \lambda_0, \tag{4}$$

$$\omega_{\log} = \exp\left[\frac{2}{\lambda} \int_{0}^{\infty} \log(\omega) \frac{\alpha^{2} F(\omega)}{\omega} d\omega\right], \tag{5}$$

$$\overline{\omega}_2 = \sqrt{\frac{2}{\lambda}} \int_0^\infty \omega \alpha^2 F(\omega) d\omega. \tag{6}$$

A third material parameter is the Coulomb pseudopotential. The effective Coulomb electron-electron interaction  $\mu$  in Migdal–Eliashberg theory differs from the Morel–Anderson pseudopotential  $\mu^*$  of McMillan's formula <sup>92</sup>. The latter is scaled to a typical phonon frequency, which we assume to be  $\overline{\omega}_2$  following ref. 58. For a given  $\mu^*$ , we can then estimate

$$\mu = [1/\mu^* - R(\overline{\omega}_2)]^{-1},\tag{7}$$

with the cutoff-dependent rescaling term<sup>90</sup>

$$R(\omega) = \frac{1}{\pi} \int_{-\infty}^{\infty} d\varepsilon \frac{N(\varepsilon)}{N(\varepsilon_F^0)} \frac{1}{\varepsilon - \varepsilon_F^0} \arctan\left[\frac{\varepsilon - \varepsilon_F^0}{\omega}\right]. \tag{8}$$

Also the fact that the summations over Matsubara frequencies are in practice truncated at a cutoff frequency  $\omega_C$  has to be considered. We limit the summations in Eqs. (1) to  $|\omega_m| < \omega_C$  and at the same time replace  $\mu$  in Eq. (1b) by  $\mu_C^* = [1/\mu + R(\omega_C)]^{-1}$  scaled to the Matsubara cutoff. Using Eq. (7), we can also write

$$\mu_C^* = [1/\mu^* - R(\overline{\omega}_2) + R(\omega_C)]^{-1}, \tag{9}$$

where  $\mu^*$  depends on doping and in multi-valley materials it also changes when calculating the inter/intra-valley repulsion. For larger doping values it has been calculated to have the mean value of  $0.13^{93}$ . In this work we therefore set  $\mu^* = 0.13$  and use it as a constant.

The Eliashberg spectral function in Eqs. (4-6) can be written as 94,95

$$\alpha^2 F(\omega) = \frac{1}{\pi N(\varepsilon_F^0)} \sum_{\mathbf{q}\nu} \frac{\gamma_{\mathbf{q}\nu}}{\omega_{\mathbf{q}\nu}} B_{\nu}(\mathbf{q}, \omega), \tag{10}$$

where  ${\bf q}$  and  ${\bf v}$  are phonon wavevector and band indices.  $\omega_{{\bf q}{\bf v}}$  are the statically screened phonon frequencies, as obtained in density functional perturbation theory (DFPT)<sup>96,97</sup>. In Eq. (10),  $\alpha^2 F(\omega)$  is written in its NA form. It can be seen as a phonon DOS, weighted, renormalized, and broadened by EPC in the form of phonon linewidths  $\gamma_{{\bf q}{\bf v}}$  obtained in the double-delta approximation<sup>98</sup> and the NA phonon spectral function

$$B_{\nu}(\mathbf{q},\omega) = -\frac{1}{\pi} \operatorname{Im} \left[ \frac{2\omega_{\mathbf{q}\nu}}{\omega^2 - \omega_{\mathbf{q}\nu}^2 - 2\omega_{\mathbf{q}\nu}\pi_{\nu}(\mathbf{q},\omega)} \right]. \tag{11}$$

With the term "adiabatic", we refer to the statically screened and infinitely long-lived (DFPT) phonons<sup>99</sup>. Nonadiabaticity refers to the fact that the statically screened DFPT phonon frequencies are corrected by the real part of the NA phonon self-energy

$$\pi_{\nu}(\mathbf{q}, \omega) = \sum_{\mathbf{k}nm} |g_{mn\nu}(\mathbf{k}, \mathbf{q})|^2 \frac{f_{n\mathbf{k}} - f_{m\mathbf{k}+\mathbf{q}}}{\omega + \varepsilon_{n\mathbf{k}} - \varepsilon_{m\mathbf{k}+\mathbf{q}} + i\eta}$$

$$- \sum_{\mathbf{k}nm} |g_{mn\nu}(\mathbf{k}, \mathbf{q})|^2 \frac{f_{n\mathbf{k}} - f_{m\mathbf{k}+\mathbf{q}}}{\varepsilon_{n\mathbf{k}} - \varepsilon_{m\mathbf{k}+\mathbf{q}}}$$
(12)

evaluated at the unrenormalized frequencies, including the broadening effects as well. In Eq. (12),  $\mathbf{q} \neq 0$ ,  $\mathbf{k}$ , and n, m are electronic momentum and band indices,  $f_{n\mathbf{k}}$  denote the Fermi-Dirac distribution functions,  $\varepsilon_{n\mathbf{k}}$  are the electron energies, and  $g_{mn\nu}(\mathbf{k}, \mathbf{q})$  are the statically screened EPC matrix elements. We use the "screened-screened" approximation to the phonon self-energy for quadratic errors<sup>64</sup>.

## Model calculations

To estimate the critical temperature for lattice distortions on very large supercells (here 2916 atoms), for which full DFPT calculations are unfeasible, we use the approximation of a linearized EPC as described in ref. 70, wherein it is referred to as "model III". Additionally, we reduce the EPC to a nearest-neighbor model including only the  $d_{z^2}$ ,  $d_{x^2-y^2}$ , and  $d_{xy}$  orbitals of the transition-metal atoms, as defined in Eq. (B4) of ref. 100 for TaS<sub>2</sub>, with parameters fitted to DFPT data for MoS<sub>2</sub>. The first-principles data are taken from Appendix B of ref. 64. Doping is modeled as a rigid shift of the chemical potential. The electronic temperature is set to 5 mRy  $\approx$  800 K. For each carrier concentration the atomic positions are optimized, starting from both a randomly distorted 2 × 2 CDW and a single triangular displacement

involving three neighboring Mo atoms, until all forces are below  $10^{-5}$  Ry/bohr. Phonons and the adiabatic effective interaction parameters are then calculated for  $\mathbf{q} = 0$  only, with the help of sparse matrices and repeated transforms between the orbital and band basis to save memory<sup>101</sup>.

#### Computational details

The written equations and their ingredients are calculated by means of DFPT% and Wannier interpolation<sup>102</sup> of EPC matrix elements<sup>103</sup>. We use Quantum ESPRESSO<sup>97</sup> for the DFT calculations, and the EPW code<sup>103–106</sup> for EPC. We use the fully-relativistic norm-conserving Perdew-Burke-Ernzerhof pseudopotentials with a kinetic energy cutoff of 100 Ry from PseudoDojo<sup>107</sup>. The NA dynamic and static terms in the phonon self-energy, Eq. (12), are calculated separately, because in the dynamic term, dense k- and q-grids are used, while the grids for the static-term calculation are already determined by the DFT and DFPT calculations  $^{23,63,108}$ . For the calculations in a 1 × 1 H phase, the relaxed lattice constant is set to 3.186 Å, with a vacuum of 16 Å. The selfconsistent electron density calculation is done on a 24 × 24 × 1 k-point grid, and the phonon calculation on a  $12 \times 12 \times 1$  **q**-point grid. In EPW, we use 11 maximally localized Wannier functions<sup>109</sup> with the initial projections of d orbitals on the Mo sites and p orbitals on the S atom sites. The fine sampling of the Brillouin zone for the electron-phonon interpolation is done on a  $360 \times 360 \times 1$  k-grid and  $120 \times 120 \times 1$  q-grid. Smearing in the EPW calculation is set to 20 meV. For the calculations in other phases, all the abovementioned parameters are the same, except that the unit cell is larger and the grids are accordingly smaller. In all the DFT and DFPT calculations, we use the Coulomb truncation<sup>110</sup>, while in the EPW calculation, we use the longrange terms which include 2D dipoles following ref. 111.

## Data availability

The most relevant data, scripts, and input files are available in the Materials Cloud Archive at <a href="https://doi.org/10.24435/materialscloud:z1-aw">https://doi.org/10.24435/materialscloud:z1-aw</a>. Further data that support the findings of this study are available from the author on reasonable request.

## Code availability

The codes for the Eliashberg and model calculations are available on Zenodo<sup>91,101</sup>. Further, browsing versions of code and data of Figs. 6 and 2e can be found at https://github.com/janberges/mos2cdwand https://github.com/janberges/mos2ebmb.

Received: 3 December 2024; Accepted: 23 April 2025; Published online: 26 May 2025

# References

- Fiori, G. et al. Electronics based on two-dimensional materials. Nat. Nanotechnol. 9, 768 (2014).
- Kumbhakar, P. et al. Prospective applications of two-dimensional materials beyond laboratory frontiers: a review. iScience 26, 106671 (2023).
- 3. Ye, J. T. et al. Superconducting dome in a gate-tuned band insulator. *Science* **338**, 1193 (2012).
- Morosan, E. et al. Superconductivity in Cu<sub>x</sub>TiSe<sub>2</sub>. Nat. Phys. 2, 544 (2006)
- Ludbrook, B. M. et al. Evidence for superconductivity in Lidecorated monolayer graphene. *Proc. Natl. Acad. Sci. USA* 112, 11795 (2015).
- Ichinokura, S., Sugawara, K., Takayama, A., Takahashi, T. & Hasegawa, S. Superconducting calcium-intercalated bilayer graphene. ACS Nano 10, 2761 (2016).
- Nagamatsu, J., Nakagawa, N., Muranaka, T., Zenitani, Y. & Akimitsu, J. Superconductivity at 39 K in magnesium diboride. *Nature* 410, 63 (2001).
- Kortus, J., Mazin, I. I., Belashchenko, K. D., Antropov, V. P. & Boyer, L. L. Superconductivity of metallic boron in MgB<sub>2</sub>. *Phys. Rev. Lett.* 86, 4656 (2001).

- Sajadi, E. et al. Gate-induced superconductivity in a monolayer topological insulator. Science 362, 922 (2018).
- Wang, X. et al. Interfacial ferroelectricity in rhombohedral-stacked bilayer transition metal dichalcogenides. *Nat. Nanotechnol.* 17, 367 (2022).
- Zheng, Z. et al. Unconventional ferroelectricity in moiré heterostructures. *Nature* 588, 71 (2020).
- Xu, Y. et al. Coexisting ferromagnetic-antiferromagnetic state in twisted bilayer Crl<sub>3</sub>. Nat. Nanotechnol. 17, 143 (2022).
- Huang, B. et al. Layer-dependent ferromagnetism in a van der Waals crystal down to the monolayer limit. Nature 546, 270 (2017).
- Bin Subhan, M. K. et al. Charge density waves in electron-doped molybdenum disulfide. Nano Lett. 21, 5516 (2021).
- Rossnagel, K. On the origin of charge-density waves in select layered transition-metal dichalcogenides. *J. Phys. Condens. Matter* 23, 213001 (2011).
- Li, J. et al. Intrinsic magnetic topological insulators in van der Waals layered MnBi<sub>2</sub>Te<sub>4</sub>-family materials. Sci. Adv. 5, eaaw5685 (2019).
- 17. Jia, Y. et al. Evidence for a monolayer excitonic insulator. *Nat. Phys.* **18.** 87 (2022).
- Mak, K. F., Lee, C., Hone, J., Shan, J. & Heinz, T. F. Atomically thin MoS<sub>2</sub>: a new direct-gap semiconductor. *Phys. Rev. Lett.* 105, 136805 (2010).
- Wang, Q. H., Kalantar-Zadeh, K., Kis, A., Coleman, J. N. & Strano, M. S. Electronics and optoelectronics of two-dimensional transition metal dichalcogenides. *Nat. Nanotechnol.* 7, 699 (2012).
- Ge, Y. & Liu, A. Y. Phonon-mediated superconductivity in electron-doped single-layer MoS<sub>2</sub>: a first-principles prediction. *Phys. Rev. B* 87, 241408(R) (2013).
- Costanzo, D., Jo, S., Berger, H. & Morpurgo, A. F. Gate-induced superconductivity in atomically thin MoS<sub>2</sub> crystals. *Nat. Nanotechnol.* 11, 339 (2016).
- Kang, M. et al. Holstein polaron in a valley-degenerate twodimensional semiconductor. *Nat. Mater.* 17, 676 (2018).
- Garcia-Goiricelaya, P., Lafuente-Bartolome, J., Gurtubay, I. G. & Eiguren, A. Long-living carriers in a strong electron-phonon interacting two-dimensional doped semiconductor. *Commun. Phys.* 2. 1 (2019).
- 24. van Efferen, C. *Growth, Phases and Correlation Effects of Single-Layer MoS*<sub>2</sub> *and VS*<sub>2</sub>. Dissertation, Universität zu Köln (2023).
- 25. van Efferen, C. et al. Inelastic tunneling into multipolaronic bound states in single-layer MoS<sub>2</sub>. https://arxiv.org/abs/2505.10972 (2024).
- Rösner, M., Haas, S. & Wehling, T. O. Phase diagram of electrondoped dichalcogenides. *Phys. Rev. B* 90, 245105 (2014).
- Piatti, E., Chen, Q., Tortello, M., Ye, J. & Gonnelli, R. S. Possible charge-density-wave signatures in the anomalous resistivity of Liintercalated multilayer MoS<sub>2</sub>. Appl. Surf. Sci. 461, 269 (2018).
- Zhuang, H. L., Johannes, M. D., Singh, A. K. & Hennig, R. G. Dopingcontrolled phase transitions in single-layer MoS<sub>2</sub>. *Phys. Rev. B* 96, 165305 (2017).
- Eda, G. et al. Photoluminescence from chemically exfoliated MoS<sub>2</sub>.
   Nano Lett. 11, 5111 (2011).
- Xiao, Y., Zhou, M., Liu, J., Xu, J. & Fu, L. Phase engineering of twodimensional transition metal dichalcogenides. *Sci. China Mater.* 62, 759 (2019).
- Zhao, W. et al. Metastable MoS<sub>2</sub>: crystal structure, electronic band structure, synthetic approach and intriguing physical properties. Chem. Eur. J. 24, 15942 (2018).
- Jin, Q., Liu, N., Chen, B. & Mei, D. Mechanisms of semiconducting 2H to metallic 1T phase transition in two-dimensional MoS<sub>2</sub> nanosheets. J. Phys. Chem. C 122, 28215 (2018).
- Lin, Y.-C., Dumcenco, D. O., Huang, Y.-S. & Suenaga, K. Atomic mechanism of the semiconducting-to-metallic phase transition in single-layered MoS<sub>2</sub>. Nat. Nanotechnol. 9, 391 (2014).

- Cheng, Y. et al. Origin of the phase transition in lithiated molybdenum disulfide. ACS Nano 8, 11447 (2014).
- Wypych, F., Weber, T. & Prins, R. Scanning tunneling microscopic investigation of 1T-MoS2<sub>2</sub>. Chem. Mater. 10, 723 (1998).
- Costanzo, D., Zhang, H., Reddy, B. A., Berger, H. & Morpurgo, A. F. Tunnelling spectroscopy of gate-induced superconductivity in MoS<sub>2</sub>. Nat. Nanotechnol. 13, 483 (2018).
- Keimer, B., Kivelson, S. A., Norman, M. R., Uchida, S. & Zaanen, J. From quantum matter to high-temperature superconductivity in copper oxides. *Nature* 518, 179 (2015).
- Paglione, J. & Greene, R. L. High-temperature superconductivity in iron-based materials. *Nat. Phys.* 6, 645 (2010).
- Koonce, C. S., Cohen, M. L., Schooley, J. F., Hosler, W. R. & Pfeiffer, E. R. Superconducting transition temperatures of semiconducting SrTiO<sub>3</sub>. Phys. Rev. 163, 380 (1967).
- Pan, X.-C. et al. Pressure-driven dome-shaped superconductivity and electronic structural evolution in tungsten ditelluride. *Nat. Commun.* 6, 7805 (2015).
- Paudyal, H., Poncé, S., Giustino, F. & Margine, E. R.
   Superconducting properties of MoTe<sub>2</sub> from ab initio anisotropic Migdal-Eliashberg theory. *Phys. Rev. B* 101, 214515 (2020).
- Setty, C., Baggioli, M. & Zaccone, A. Superconducting dome in ferroelectric-type materials from soft mode instability. *Phys. Rev. B* 105, L020506 (2022).
- Appel, J. Soft-mode superconductivity in SrTiO<sub>3-x</sub>. Phys. Rev. 180, 508 (1969).
- Edge, J. M., Kedem, Y., Aschauer, U., Spaldin, N. A. & Balatsky, A. V.
   Quantum critical origin of the superconducting dome in SrTiO<sub>3</sub>.
   Phys. Rev. Lett. 115, 247002 (2015).
- Yang, W. et al. Soft-mode-phonon-mediated unconventional superconductivity in monolayer 1T'-WTe<sub>2</sub>. Phys. Rev. Lett. 125, 237006 (2020).
- Ma, J., Yang, R. & Chen, H. A large modulation of electron-phonon coupling and an emergent superconducting dome in doped strong ferroelectrics. *Nat. Commun.* 12, 2314 (2021).
- Das, T. & Dolui, K. Superconducting dome in MoS<sub>2</sub> and TiSe<sub>2</sub> generated by quasiparticle-phonon coupling. *Phys. Rev. B* 91, 094510 (2015).
- Joe, Y. I. et al. Emergence of charge density wave domain walls above the superconducting dome in 1T-TiSe<sub>2</sub>. Nat. Phys. 10, 421 (2014).
- Kusmartseva, A. F., Sipos, B., Berger, H., Forró, L. & Tutiš, E. Pressure induced superconductivity in pristine 1T-TiSe<sub>2</sub>. Phys. Rev. Lett. 103, 236401 (2009).
- Johannes, M. D. & Mazin, I. I. Fermi surface nesting and the origin of charge density waves in metals. *Phys. Rev. B* 77, 165135 (2008).
- Yu, F. H. et al. Unusual competition of superconductivity and charge-density-wave state in a compressed topological kagome metal. *Nat. Commun.* 12, 3645 (2021).
- 52. Zhu, H. & Han, H. Charge density wave in low dimensional materials. *J. Phys. Conf. Ser.* **2338**, 012028 (2022).
- Morris, R. C. Connection between charge-density waves and superconductivity in NbSe<sub>2</sub>. Phys. Rev. Lett. 34, 1164 (1975).
- Gabovich, A. M., Voitenko, A. I., Annett, J. F. & Ausloos, M. Chargeand spin-density-wave superconductors. *Supercond. Sci. Technol.* 14, R1 (2001).
- Nagata, S. et al. Superconductivity in the layered compound 2H-TaS<sub>2</sub>. J. Phys. Chem. Solids 53, 1259 (1992).
- Eliashberg, G. M. Interactions between electrons and lattice vibrations in a superconductor. Sov. Phys. JETP 11, 696 (1960).
- McMillan, W. L. Transition temperature of strong-coupled superconductors. *Phys. Rev.* 167, 331 (1968).
- Allen, P. B. & Dynes, R. C. Transition temperature of strong-coupled superconductors reanalyzed. *Phys. Rev. B* 12, 905 (1975).

- 59. Fu, Y. et al. Gated tuned superconductivity and phonon softening in monolayer and bilayer MoS<sub>2</sub>, npi Quant. Mater. **2.** 1 (2017).
- Setty, C., Baggioli, M. & Zaccone, A. Anharmonic theory of superconductivity and its applications to emerging quantum materials. J. Phys. Condens. Matter 36, 173002 (2024).
- 61. Margine, E. R. & Giustino, F. Anisotropic Migdal-Eliashberg theory using Wannier functions. *Phys. Rev. B* **87**, 024505 (2013).
- Marini, G. & Calandra, M. Phonon mediated superconductivity in field-effect doped molybdenum dichalcogenides. 2D Mater. 10, 015013 (2022).
- Girotto, N. & Novko, D. Dynamical renormalization of electronphonon coupling in conventional superconductors. *Phys. Rev. B* 107, 064310 (2023).
- Berges, J., Girotto, N., Wehling, T., Marzari, N. & Poncé, S. Phonon self-energy corrections: to screen, or not to screen. *Phys. Rev. X* 13, 041009 (2023).
- Novko, D. Broken adiabaticity induced by Lifshitz transition in MoS<sub>2</sub> and WS<sub>2</sub> single layers. Commun. Phys. 3, 30 (2020).
- Yuan, N. F. Q., Mak, K. F. & Law, K. T. Possible topological superconducting phases of MoS<sub>2</sub>. *Phys. Rev. Lett.* 113, 097001 (2014).
- Lu, J. M. et al. Evidence for two-dimensional Ising superconductivity in gated MoS<sub>2</sub>. Science 350, 1353 (2015).
- Zhou, B. T., Yuan, N. F. Q., Jiang, H.-L. & Law, K. T. Ising superconductivity and majorana fermions in transition-metal dichalcogenides. *Phys. Rev. B* 93, 180501 (2016).
- Zheliuk, O. et al. Josephson coupled Ising pairing induced in suspended MoS<sub>2</sub> bilayers by double-side ionic gating. *Nat. Nanotechnol.* 14, 1123 (2019).
- Schobert, A. et al. Ab initio electron-lattice downfolding: potential energy landscapes, anharmonicity, and molecular dynamics in charge density wave materials. SciPost Phys. 16, 046 (2024).
- Di Salvo, F. J., Moncton, D. E. & Waszczak, J. V. Electronic properties and superlattice formation in the semimetal TiSe<sub>2</sub>. Phys. Rev. B 14, 4321 (1976).
- Gan, X. et al. 2H/1T phase transition of multilayer MoS<sub>2</sub> by electrochemical incorporation of S vacancies. ACS Appl. Energy Mater. 1, 4754 (2018).
- Friedman, A. L. et al. Evidence for chemical vapor induced 2H to 1T phase transition in MoX<sub>2</sub> (X = Se, S) transition metal dichalcogenide films. Sci. Rep. 7, 3836 (2017).
- Huang, H. H., Fan, X., Singh, D. J. & Zheng, W. T. First principles study on 2H-1T' transition in MoS<sub>2</sub> with copper. *Phys. Chem. Chem. Phys.* 20, 26986 (2018).
- Tan, S. J. R. et al. Temperature- and phase-dependent phonon renormalization in 1T'-MoS<sub>2</sub>. ACS Nano 12, 5051 (2018).
- Sohier, T. et al. Enhanced electron-phonon interaction in multivalley materials. *Phys. Rev. X* 9, 031019 (2019).
- Garcia-Goiricelaya, P., Lafuente-Bartolome, J., Gurtubay, I. G. & Eiguren, A. Emergence of large nonadiabatic effects induced by the electron-phonon interaction on the complex vibrational quasiparticle spectrum of doped monolayer MoS<sub>2</sub>. Phys. Rev. B 101, 054304 (2020).
- Zhang, R. et al. Superconductivity in potassium-doped metallic polymorphs of MoS<sub>2</sub>. Nano Lett. 16, 629 (2016).
- Holtgrewe, K., Marini, G. & Calandra, M. Light-induced polaronic crystals in single-layer transition metal dichalcogenides. *Nano Lett.* 24, 13179–13184 (2024).
- Kim, J.-H., Schönhoff, G., Lorke, M., Wehling, T. O. & Yee, K.-J. Ultrafast reversible phase engineering in MoTe<sub>2</sub> thin film via polaron formation. J. Korean Phys. Soc. 84, 907 (2024).
- Ortenzi, L., Pietronero, L. & Cappelluti, E. Zero-point motion and direct-indirect band-gap crossover in layered transition-metal dichalcogenides. *Phys. Rev. B* 98, 195313 (2018).

- Veld, Y. I., Katsnelson, M. I., Millis, A. J. & Rösner, M. Screening induced crossover between phonon- and plasmon-mediated pairing in layered superconductors. 2D Mater. 10, 045031 (2023).
- Sohier, T., Gibertini, M., Martin, I. & Morpurgo, A. F. Unconventional gate-induced superconductivity in transition-metal dichalcogenides. *Phys. Rev. Research* 7, 013290 (2025).
- Lu, J. et al. Full superconducting dome of strong Ising protection in gated monolayer WS<sub>2</sub>. Proc. Natl. Acad. Sci. USA 115, 3551 (2018).
- 85. Anderson, P. W., Muttalib, K. A. & Ramakrishnan, T. V. Theory of the "universal" degradation of  $T_c$  in high-temperature superconductors. *Phys. Rev. B* **28**, 117 (1983).
- Testardi, L. R. Structural instability, anharmonicity, and hightemperature superconductivity in A-15-structure compounds. *Phys. Rev. B* 5, 4342 (1972).
- Allen, P. B. Effect of soft phonons on superconductivity: a reevaluation and a positive case for Nb<sub>2</sub>Sn. Solid State Commun. 14, 937 (1974).
- Bardeen, J., Cooper, L. N. & Schrieffer, J. R. Theory of superconductivity. *Phys. Rev.* 108, 1175 (1957).
- Marsiglio, F. Eliashberg theory of the critical temperature and isotope effect. Dependence on bandwidth, band-filling, and direct Coulomb repulsion. J. Low Temp. Phys. 87, 659 (1992).
- Berges, J. On the Scope of McMillan's Formula. Master's thesis, Universität Bremen (2016).
- 91. Berges, J. ebmb: solve multiband Eliashberg equations. *Zenodo* https://doi.org/10.5281/zenodo.13341224 (2016).
- Morel, P. & Anderson, P. W. Calculation of the superconducting state parameters with retarded electron-phonon interaction. *Phys. Rev.* 125, 1263 (1962).
- Schönhoff, G., Rösner, M., Groenewald, R. E., Haas, S. & Wehling, T.
   Interplay of screening and superconductivity in low-dimensional materials. *Phys. Rev. B* 94, 134504 (2016).
- Allen, P. B. & Silberglitt, R. Some effects of phonon dynamics on electron lifetime, mass renormalization, and superconducting transition temperature. *Phys. Rev. B* 9, 4733 (1974).
- Allen, P. B. & Mitrović, B. Theory of Superconducting T<sub>c</sub>. In Solid State Physics: Advances in Research and Applications (eds Ehrenreich, H., Seitz, F. & Turnbull, D.) 1–92 (Academic Press, 1982).
- Baroni, S., de Gironcoli, S., Dal Corso, A. & Giannozzi, P. Phonons and related crystal properties from density-functional perturbation theory. *Rev. Mod. Phys.* 73, 515 (2001).
- Giannozzi, P. et al. QUANTUM ESPRESSO: a modular and opensource software project for quantum simulations of materials. *J. Phys. Condens. Matter* 21, 395502 (2009).
- Allen, P. B. Neutron spectroscopy of superconductors. *Phys. Rev. B* 6, 2577 (1972).
- Marini, A. Nonadiabatic effects lead to the breakdown of the semiclassical phonon picture. *Phys. Rev. B* 110, 024306 (2024).
- 100. Berges, J., van Loon, E. G. C. P., Schobert, A., Rösner, M. & Wehling, T. O. Ab initio phonon self-energies and fluctuation diagnostics of phonon anomalies: Lattice instabilities from Dirac pseudospin physics in transition metal dichalcogenides. *Phys. Rev. B* 101, 155107 (2020).
- Berges, J., Schobert, A., van Loon, E. G. C. P., Rösner, M. & Wehling, T. O. elphmod: Python modules for electron-phonon models. Zenodo https://doi.org/10.5281/zenodo.5919991 (2017).
- Mostofi, A. A. et al. wannier90: a tool for obtaining maximallylocalised Wannier functions. *Comput. Phys. Commun.* 178, 685 (2008).
- Poncé, S., Margine, E., Verdi, C. & Giustino, F. EPW: electronphonon coupling, transport and superconducting properties using maximally localized Wannier functions. *Comput. Phys. Commun.* 209, 116 (2016).
- Giustino, F., Cohen, M. L. & Louie, S. G. Electron-phonon interaction using Wannier functions. *Phys. Rev. B* 76, 165108 (2007).

- Noffsinger, J. et al. EPW: a program for calculating the electronphonon coupling using maximally localized Wannier functions. Comput. Phys. Commun. 181, 2140 (2010).
- Lee, H. et al. Electron-phonon physics from first principles using the EPW code. npj Comput. Mater. 9, 1 (2023).
- van Setten, M. J. et al. The PseudoDojo: training and grading a 85 element optimized norm-conserving pseudopotential table.
   Comput. Phys. Commun 226, 39 (2018).
- Novko, D. Nonadiabatic coupling effects in MgB<sub>2</sub> reexamined. *Phys. Rev. B* 98, 041112(R) (2018).
- Marzari, N., Mostofi, A. A., Yates, J. R., Souza, I. & Vanderbilt, D. Maximally localized Wannier functions: theory and applications. *Rev. Mod. Phys.* 84, 1419 (2012).
- Sohier, T., Calandra, M. & Mauri, F. Density functional perturbation theory for gated two-dimensional heterostructures: theoretical developments and application to flexural phonons in graphene. *Phys. Rev. B* **96**, 075448 (2017).
- Poncé, S., Royo, M., Stengel, M., Marzari, N. & Gibertini, M. Longrange electrostatic contribution to electron-phonon couplings and mobilities of two-dimensional and bulk materials. *Phys. Rev. B* 107, 155424 (2023).

#### **Acknowledgements**

Useful discussions with Raffaello Bianco and Ivor Lončarić are gratefully acknowledged. N.G.E. and D.N. acknowledge financial support from the Croatian Science Foundation (Grant no. UIP-2019-04-6869) and from the project "Podizanje znanstvene izvrsnosti Centra za napredne laserske tehnike (CALTboost)" financed by the European Union through the National Recovery and Resilience Plan 2021-2026 (NRPP). J.B. acknowledges support from the Deutsche Forschungsgemeinschaft (DFG) under Germany's Excellence Strategy (University Allowance, EXC 2077, University of Bremen), computing time granted by the Resource Allocation Board and provided on the supercomputer Emmy/Grete at NHR-Nord@Goettingen as part of the NHR infrastructure, and fruitful discussions with Tim O. Wehling, Arne Schobert, and Laura Paetzold, S.P. acknowledges support from the Fonds de la Recherche Scientifique de Belgique (FRS-FNRS) and by the Walloon Region in the strategic axe FRFS-WEL-T. Computational resources have been provided by the PRACE award, granting access to MareNostrum4 at Barcelona Supercomputing Center (BSC), Spain, and Discoverer in Sofia-Tech, Bulgaria (OptoSpin project id. 2020225411).

#### **Author contributions**

N.G.E. and D.N. conceived the project. N.G.E. performed the DFT theoretical calculations, wrote the first draft of the manuscript, and made the corresponding figures. J.B. performed the TBA model calculations, and made the corresponding figures. All authors discussed the results, and were involved in the writing and reviewing of the manuscript. D.N. and S.P. supervised the project.

# Competing interests

The authors declare no competing interests.

#### **Additional information**

**Supplementary information** The online version contains supplementary material available at https://doi.org/10.1038/s41699-025-00563-3.

**Correspondence** and requests for materials should be addressed to Nina Girotto Erhardt or Dino Novko.

**Reprints and permissions information** is available at http://www.nature.com/reprints

**Publisher's note** Springer Nature remains neutral with regard to jurisdictional claims in published maps and institutional affiliations.

Open Access This article is licensed under a Creative Commons Attribution-NonCommercial-NoDerivatives 4.0 International License, which permits any non-commercial use, sharing, distribution and reproduction in any medium or format, as long as you give appropriate credit to the original author(s) and the source, provide a link to the Creative Commons licence, and indicate if you modified the licensed material. You do not have permission under this licence to share adapted material derived from this article or parts of it. The images or other third party material in this article are included in the article's Creative Commons licence, unless indicated otherwise in a credit line to the material. If material is not included in the article's Creative Commons licence and your intended use is not permitted by statutory regulation or exceeds the permitted use, you will need to obtain permission directly from the copyright holder. To view a copy of this licence, visit <a href="http://creativecommons.org/licenses/by-nc-nd/4.0/">http://creativecommons.org/licenses/by-nc-nd/4.0/</a>.

© The Author(s) 2025